Theoretical Studies of the Spin Dynamics of Quadrupolar Nuclei at Rotational Resonance Conditions.

Jamie D. Walls, Kwang Hun Lim, and Alexander Pines

Materials Sciences Division, Lawrence Berkeley National Laboratory and
Department of Chemistry, University of California at Berkeley, Berkeley, CA 94720, USA

ABSTRACT

A theory of the spin dynamics of I=3/2 quadrupolar nuclei in the sudden-passage limit is discussed in relation to the recently observed rotational resonance (RR) effects on the excitation and conversion of triple-quantum coherence in the FASTER multiple-quantum magic-angle spinning (MQMAS) experiments [T. Vosegaard, P. Florian, D. Massiot, and P. J. Grandinetti, J. Chem. Phys. **114**, 4618 (2001)]. A novel interaction frame, which combines the quadrupolar interaction with the central transition radio frequency irradiation, is shown to be useful in understanding the complex spin dynamics at and away from RR conditions. Analytical expressions for the Hamiltonian obtained from bimodal Floquet theory are included in order to provide insight into the spin dynamics observed in the FASTER MQMAS experiments. Numerical simulations have been performed and were found to support the theoretical formalism.

I. INTRODUCTION

The study of the spin dynamics of quadrupolar nuclei in rotating samples is an important and active area of research in solid state NMR. The spin dynamics of a quadrupolar spin under magic-angle spinning (MAS) conditions is drastically different from that of non-quadrupolar spin systems. The large, time-dependent quadrupolar interaction complicates the spin dynamics, rendering quadrupolar nuclei unsuitable as a practical magnetization source in the cross-polarization MAS experiments for which efficient spin-locking of the magnetization is essential. In addition, the recently developed high-resolution multiple-quantum magic-angle spinning (MQMAS) technique[1, 2] for half-integer quadrupolar nuclei has drawn more attention to the study of the spin dynamics of quadrupolar nuclei, in order to improve efficiency of the multiple-quantum excitation and subsequent conversion to central transition coherences.

In 1992, A. J. Vega formulated a theory regarding the spin-locking behavior of the central transition (CT) coherence in quadrupolar spin systems.[3, 4] The theory demonstrated that the spin-locking behavior is strongly dependent on the relationship between the magnitude of the quadrupolar interaction (ω_Q), the spinning frequency (ω_r), and the radio frequency (rf) field strength (ω_1). Vega introduced an adiabaticity parameter, $\alpha = \dfrac{\omega_1^2}{\omega_Q \omega_r}$, to characterize the spin-locking behavior as a function of the rf power. In the adiabatic region, where high rf power is applied under slow MAS (i.e., $\alpha \gg 1$), conversion from CT to multiple-quantum (MQ) transition coherence occurs during the spin-locking pulse and sample rotation. Such transfers are the basis of the RIACT

method used in MQMAS sequences for MQ conversions.[5] Under conditions of low rf power and rapid sample spinning (i.e., the sudden-passage limit where $\alpha \ll 1$), the CT coherences are not transferred into MQ coherences, thus the CT coherences are effectively spin-locked. However, when at rotational resonance (RR) conditions given by

$\omega_1 = \dfrac{n\omega_r}{I+1/2}$ [6,7] (where I is the spin quantum number of the quadrupolar nucleus and n is an integer), poor spin-locking behavior in the sudden-passage limit is observed. This phenomenon has not been well understood.

More recently, Vosegaard et al.[8] observed interesting coherence transfers in I=3/2 nuclei at low rf power and under fast MAS, a technique called the FASTER MQMAS experiment. They demonstrated that triple-quantum coherence could be created efficiently from triple-quantum z-magnetization when spin-locking between the conditions $(n-1)\omega_r < 2\omega_1 < n\omega_r$, with minimum efficiency occurring at $2\omega_1 = n\omega_r$. Additionally, triple-quantum coherence was efficiently transferred to CT coherence at RR conditions, $\omega_1 = n\omega_r$. This may explain the poor spin-locking efficiency of the CT coherence at RR conditions. However, a rigorous theoretical treatment is required in order to understand fully the complicated spin dynamics in the sudden-passage limit. Such an understanding would be useful in the design of other low rf power multiple-quantum excitation and conversion schemes.

In this report, we present a new theoretical approach that explains the two types of coherence transfers exploited in the FASTER MQMAS experiments.[8] An interaction frame involving both the quadrupolar and CT Hamiltonians is used in order to obtain quantitative insight into the spin dynamics. A perturbative treatment using bimodal

Floquet theory[9] is then employed to explore the spin dynamics of I=3/2 nuclei in the sudden-passage regime.

II. THEORY

A. Hamiltonian in the interaction frame

Under rf irradiation and neglecting resonance offsets and the second-order quadrupolar interaction, the rotating-frame spin Hamiltonian of a spin I=3/2 nucleus during MAS can be written in a fictitious spin ½ operator[10, 11] basis as:

$$H(t) = \omega_Q(t)(I_Z^{1-2} - I_Z^{3-4}) + \sqrt{3}\omega_1(I_X^{1-2} + I_X^{3-4}) + 2\omega_1 I_X^{2-3}$$

$$= H_Q(t) + H_{RF}^{ST} + H_{RF}^{CT} \qquad [1]$$

where ω_1 is the rf field strength. The states are labeled as $|1\rangle = |m_I = +3/2\rangle$, $|2\rangle = |m_I = +1/2\rangle$, $|3\rangle = |m_I = -1/2\rangle$, and $|4\rangle = |m_I = -3/2\rangle$. The first-order quadrupolar frequency, $\omega_Q(t)$, which is rendered time-dependent by MAS, is given by:

$$\omega_Q(t) = \omega_Q[C_1\cos(\omega_r t + \gamma) + C_2\cos(2\omega_r t + 2\gamma) + S_1\sin(\omega_r t + \gamma) + S_2\sin(2\omega_r t + 2\gamma)]$$

$$C_1 = -\frac{3}{8}\sin(2\theta)\sin(2\beta)\left(1 - \frac{\eta}{3}\cos(2\alpha)\right)$$

$$C_2 = \frac{3}{8}\sin^2(\theta)\left(\sin^2(\beta) + \frac{\eta}{3}(\cos^2(\beta) + 1)\cos(2\alpha)\right)$$

$$S_1 = -\frac{\eta}{4}\sin(2\theta)\sin(\beta)\sin(2\alpha)$$

$$S_2 = -\frac{\eta}{4}\sin^2(\theta)\cos(\beta)\sin(2\alpha)$$

$$\omega_Q = 2\pi \frac{3C_Q}{I(2I-1)} \tag{2}$$

where $C_Q = \frac{e^2qQ}{h}$ is the quadrupolar coupling constant, and η is the quadrupolar asymmetry parameter. The Euler angles (α, β, γ) relate the quadrupolar principal axis system to the rotor-fixed coordinate system, and $\theta = \cos^{-1}\left(\frac{1}{\sqrt{3}}\right)$, the magic-angle. The propagator for the Hamiltonian is given by:

$$U(t) = T\left\{\exp(-i\int_0^t H(t')dt')\right\} \tag{3}$$

where T is the Dyson time ordering operator. The dynamics of spin 3/2 nuclei under spin-locking conditions has been studied in the past.[12, 13] The dynamics of the system are complicated by the large, time-dependent quadrupolar Hamiltonian, which does not commute at different times with the satellite transition term, H_{RF}^{ST}, of the rf Hamiltonian. In such cases, a quadrupolar interaction frame has been used in order to remove the quadrupolar term from subsequent calculations in the new frame. This has been utilized in the past under both static[14] and MAS conditions[15] to explain many phenomena in systems with large quadrupole moments.

Consider an alternative transformation defined by

$$V(t) = T\left\{\exp\left(-i\int_0^t \left[H_Q(t') + H_{RF}^{CT}\right]dt'\right)\right\}$$

$$= \exp[-i \int_0^t \omega_Q(t')dt'(I_Z^{1-2} - I_Z^{3-4})]\exp(-2i\omega_1 t I_X^{2-3}) \qquad [4]$$

The first exponential term represents the ordinary transformation into the quadrupolar frame. The second exponential term is an additional piece involving only the CT spin operator. Since both terms commute with each other at different times, V(t) can be evaluated easily by simple integration. The inclusion of the CT in the frame transformation makes the mechanism of RR in quadrupolar spin systems more transparent.

Eq. [3] then can be rewritten as

$$U(t) = V(t)\, T\left\{\exp(-i \int_0^t H_{Q,CT}(t')dt')\right\} = V(t)U_{Q,CT}(t) \qquad [5]$$

where $U_{Q,CT}(t)$ is the propagator in the interaction frame, generated by the Hamiltonian $H_{Q,CT}(t)$:

$$H_{Q,CT}(t) = V^\dagger(t)H(t)V(t) - iV^\dagger(t)\frac{d(V(t))}{dt}$$

$$= \sqrt{3}\omega_1 \left\{[(I_X^{1-2} + I_X^{3-4})\cos(\omega_1 t) + (I_Y^{1-3} - I_Y^{2-4})\sin(\omega_1 t)]\cos(\int_0^t \omega_Q(t')dt') - \right.$$

$$\left. [(I_Y^{1-2} - I_Y^{3-4})\cos(\omega_1 t) - (I_X^{1-3} + I_X^{2-4})\sin(\omega_1 t)]\sin(\int_0^t \omega_Q(t')dt')\right\} \qquad [6]$$

In this frame, the satellite transitions are modulated at ω_1 from the CT Hamiltonian and at ω_r from the modulation of the quadrupolar interaction under MAS.

Since $\omega_Q(t) = \omega_Q(t + 2\pi/\omega_r)$,

$$\cos(\int_0^t \omega_Q(t')dt') = \sum_{n=-\infty}^{\infty} A_n \exp(in\omega_r t)$$

$$\sin\left(\int_0^t \omega_Q(t')dt'\right) = \sum_{n=-\infty}^{\infty} B_n \exp(in\omega_r t)$$

[7]

Therefore, Eq. [6] can be expanded in a Fourier series in both ω_1 and ω_r to give:

$$H_{Q,CT} = \sum_{m=\pm 1} \sum_{n=-\infty}^{\infty} H_{n,m} \exp(-im\omega_1 t)\exp(-in\omega_r t)$$

[8]

where

$$H_{n,\pm 1} = \frac{\sqrt{3}}{2}\omega_1\left[\left(I_X^{1-2} + I_X^{3-4}\right)A_n - \left(I_Y^{1-2} - I_Y^{3-4}\right)B_n\right.$$

$$+ \exp\left(\mp i\frac{\pi}{2}\right)\left(\left(I_Y^{1-3} - I_Y^{2-4}\right)A_n + \left(I_X^{1-3} + I_X^{2-4}\right)B_n\right)\right]$$

$$= \frac{\sqrt{3}}{2}\omega_1\left(\left(A_n + iB_n\right)|T\mp\rangle\langle C\mp| + \left(A_n - iB_n\right)|C\pm\rangle\langle T\pm|\right)$$

[9]

where $|T\pm\rangle = \frac{1}{\sqrt{2}}\left(|1\rangle \pm |4\rangle\right)$ and $|C\pm\rangle = \frac{1}{\sqrt{2}}\left(|2\rangle \pm |3\rangle\right)$ are the triple-quantum and CT

states, as previously defined by Vega.[3] In order to evaluate the propagator of Eq. [5], bimodal Floquet theory is utilized. In the past, Floquet theory has been used in the study quadrupolar nuclei under spin-locking and MAS.[12, 16] From Eq. [8], two natural frequencies, ω_r (from the MAS) and ω_1 (from the CT rf), arise in the problem, thus necessitating the use of bimodal Floquet theory.[9] In the next section, bimodal Floquet theory is used to solve for $U_{Q,CT}(t)$, the propagator in the interaction frame.

B. Bimodal Floquet Treatment

The time dependence of the Hamiltonian complicates the evaluation of $U_{Q,CT}(t)$ since $[H_{Q,CT}(t), H_{Q,CT}(t')] \neq 0$ for $t \neq t'$ but can be removed by transforming to Floquet space. However, this requires expanding a four dimensional Hilbert space to an infinite dimensional Floquet space.[17] In this space, the spin states, $|p\rangle = |T\pm\rangle, |C\pm\rangle$, become "dressed" with the states $|N, M\rangle$, which are "oscillator-like" states labeled by the number of quadrupolar-induced rotational quanta and CT rf quanta, respectively. A Floquet Hamiltonian then can be written

$$H_F = \sum_p \sum_{N=-\infty}^{\infty} \sum_{M=-\infty}^{\infty} \left(\begin{array}{l} E_{N,M}|p,N,M\rangle\langle p,N,M| + \sum_{p'} \langle p|H_{0,1}|p'\rangle |p,N,M+1\rangle\langle p',N,M| + \\[2mm] \langle p|H_{0,-1}|p'\rangle |p,N,M\rangle\langle p',N,M+1| + \sum_{n=1}^{\infty} \langle p|H_{n,1}|p'\rangle |p,N+n,M+1\rangle\langle p',N,M| + \\[2mm] \langle p|H_{-n,-1}|p'\rangle |p,N,M\rangle\langle p',N+n,M+1| + \langle p|H_{n,-1}|p'\rangle |p,N+n,M-1\rangle\langle p',N,M| + \\[2mm] \langle p|H_{-n,1}|p'\rangle |p,N,M\rangle\langle p',N+n,M-1| \end{array} \right)$$

$$= \omega_r N^r + \omega_1 N^1 + \left(\begin{array}{l} H_{0,1}b^\dagger + H_{0,-1}b + \sum_{n=1}^{\infty} H_{n,1}(a^\dagger)^n b^\dagger \\[2mm] + H_{-n,-1}a^n b + H_{-n,1}a^n b^\dagger + H_{n,-1}(a^\dagger)^n b \end{array} \right) \qquad [11]$$

where $E_{N,M} \equiv \omega_r N + \omega_1 M$, and the operators $H_{n,\pm 1}$ are defined in Eq. [9]. N^r and N^1 act similarly to number operators for the rotational and CT quanta respectively, and the operators a, $a^\dagger$, b, $b^\dagger$ act similarly to raising and lowering operators for the rotational and CT "quanta" respectively. Their matrix elements are given by

$$\langle p,N,M|\omega_r N^r + \omega_1 N^1|p',N',M'\rangle = \delta_{p,p'}\delta_{N,N'}\delta_{M,M'}E_{N,M}$$

$$\langle p,N,M|H_{m,\pm 1}a^n|p',N',M'\rangle = \langle p|H_{m,\pm 1}|p'\rangle\delta_{N,N'-n}\delta_{M,M'}$$

$$\langle p,N,M|H_{m,\pm 1}(a^\dagger)^n|p',N',M'\rangle = \langle p|H_{m,\pm 1}|p'\rangle\delta_{N,N'+n}\delta_{M,M'}$$

$$\langle p, N, M | H_{m,\pm 1} b^n | p', N', M' \rangle = \langle p | H_{m,\pm 1} | p' \rangle \delta_{N,N'} \delta_{M,M'-n}$$

$$\langle p, N, M | H_{m,\pm 1} (b^\dagger)^n | p', N', M' \rangle = \langle p | H_{m,\pm 1} | p' \rangle \delta_{N,N'} \delta_{M,M'+n} \qquad [12]$$

Eq. [3] then can be written as:

$$U(t) = V(t) \exp(-iH_F t) \qquad [13]$$

In the following sections, nondegenerate and degenerate perturbation theories will be used to gain quantitative insight into the spin dynamics of quadrupolar nuclei at and away from RR conditions.

1. Away from Rotational Resonance Conditions

Away from RR conditions, the states $|p, N, M\rangle$ and $|p', N', M \pm 1\rangle$ are not degenerate with respect to rf and rotational energies, i.e. $E_{N,M} \neq E_{N',M\pm 1}$. Therefore, non-degenerate perturbation theory can be used to evaluate H_F by treating the $H_{n,\pm 1}$ terms as a perturbation to the $\omega_r N^r + \omega_1 N^1$ term. The validity of a perturbation expansion requires that the energy difference between the states that are coupled by the perturbation be greater in magnitude than the coupling. Formally this requires

$$\left| E_{N,M} - E_{N',M'} \right| > Z \left| H_{N-N',M-M'} \right| \qquad [14]$$

for all possible N, M, N', M', and $Z \geq 1$. Since $H_{N-N',M-M'}$ is nonzero only if $M - M' = \pm 1$, this gives

$$\left| (N - N')\omega_r \pm \omega_1 \right| > Z \left| H_{N-N',\pm 1} \right| = Z \frac{\sqrt{3}\omega_1}{2} \left| A_{N-N'} \pm iB_{N-N'} \right| \qquad [15]$$

Fig. 1 gives the fraction of crystallite orientations that satisfy Eq. [15] for $Z = 2$ [(a), (b)] and $Z = 4$ [(c), (d)], under two different sample spinning speeds, $\omega_r/2\pi = 20$ kHz [(a), (c)] and 40 kHz [(b), (d)], with $C_Q = 2.43$ MHz and $\eta = 0$. As shown in Fig. 1, the fraction of

crystallites satisfying the perturbation criterion decreases with increasing rf power and decreasing ω_Q/ω_r. Also, the larger the ratio of ω_Q/ω_r, the more RR conditions will be observed. In addition, dips appear at the RR conditions $n\omega_r = \omega_1$. This stems from the fact that the states $|T\pm, N, M\rangle$ and $|C\pm, N+n, M-1\rangle$ are degenerate, and therefore H_F must be explicitly diagonalized in these subspaces. This results in a mixing triple-quantum and CT states and is the basis for the triple-quantum conversions observed under RR, as will be discussed in the next section. Although the energy difference between the Floquet states is greater than the coupling between them for the majority of crystallite orientations, Fig. 1 indicates that it is not much bigger. This means that higher-order terms in the perturbation treatment must be calculated in order to fully describe the dynamics. In the following treatment, we present calculations only up to second-order. Using the fact that $[H_{N,\pm1}, H_{P,\pm1}] = 0$ for all N and P, H_F can be written to second-order as[9, 18]

$$
H_F = \sum_{N=-\infty}^{\infty} \sum_{M=-\infty}^{\infty} \left[\sum_p E_{N,M} |p,N,M\rangle\langle p,N,M| + \frac{1}{2} \sum_{D=-\infty}^{\infty} \sum_{S=\pm1} \frac{[H_{D,S}, H_{-D,-S}]}{D\omega_r + S\omega_1} |N,M\rangle\langle N,M| \right]
$$

$$
= \sum_{N=-\infty}^{\infty} \sum_{M=-\infty}^{\infty} \left[\begin{array}{c} \omega_r N + \omega_1 M + \sum_{D=-\infty}^{\infty} \frac{3i\omega_1^2 (I_z^{1-2} - I_z^{3-4})(A_{-D}B_D - A_D B_{-D})}{2(D\omega_r + \omega_1)} - \\ \frac{3\omega_1^2 (I_x^{1-4} - I_x^{2-3})(A_D A_{-D} + B_D B_{-D})}{2(D\omega_r + \omega_1)} \end{array} \right] |N,M\rangle\langle N,M|
$$

$$
= \sum_{N=-\infty}^{\infty} \sum_{M=-\infty}^{\infty} (\omega_r N + \omega_1 M)(|T+\rangle\langle T+| + |T-\rangle\langle T-| + |C+\rangle\langle C+| + |C-\rangle\langle C-|)|N,M\rangle\langle N,M|
$$

$$
+ \sum_{D=-\infty}^{\infty} \frac{3i\omega_1^2(|T+\rangle\langle T+| + |T-\rangle\langle T-| - |C+\rangle\langle C+| - |C-\rangle\langle C-|)(A_D B_{-D} - A_{-D}B_D)}{4(D\omega_r + \omega_1)} |N,M\rangle\langle N,M|
$$

$$
+ \frac{3\omega_1^2(|T-\rangle\langle T-| - |T+\rangle\langle T+| - |C-\rangle\langle C-| + |C+\rangle\langle C+|)(A_D A_{-D} + B_D B_{-D})}{4(D\omega_r + \omega_1)} |N,M\rangle\langle N,M|
$$

To this order of perturbation theory, the eigenstates of H_F are given by $|T\pm\rangle|N,M\rangle$ and

$|C\pm\rangle|N,M\rangle$.   In the absence of any second-order quadrupolar coupling and resonance

offset, the density matrix at time t is given by

$$\rho(t) = 3\left(I_Z^{1-4}\cos(\omega_{nut}t) - I_Y^{1-4}\sin(\omega_{nut}t)\right) \tag{17}$$

with the initial condition $\rho(0)=3\,I_Z^{1-4}$.   This simply describes the nutation of initial

populations, given by I_Z^{1-4}, into triple-quantum coherences.   The nutation frequency is

given by:

$$\omega_{nut} = -\frac{3\omega_1(A_0^2 + B_0^2)}{2} + \sum_{D=1}^{\infty}\frac{3\omega_1^3\left(A_D A_{-D} + B_D B_{-D}\right)}{D^2\omega_r^2 - \omega_1^2} \tag{18}$$

Without the second-order quadrupolar coupling, Eq. [17] indicates that only I_Y^{1-4} is

generated for all crystallite orientations, i.e., only y-phase triple-quantum coherence is

excited for each crystallite.   This explains why the creation of triple-quantum coherence

is enhanced away from RR.   However, when halfway between RR conditions, there is a

minimum in the efficiency of triple-quantum coherence creation.[8] Using Eq. [18], a

distribution for ω_{nut} over different crystallites can be calculated for a powder at various rf

field strengths, as shown in Fig. 2.   From this figure, it can be seen that the powder

averaged $\overline{\omega_{nut}}$ should change signs in between RR conditions.   When $\omega_1 \approx (n+1/2)\omega_r$,

$\overline{\omega_{nut}} = 0$, with the distribution of ω_{nut} becoming more symmetric about $\omega_{nut} = 0$, thus

degrading the efficiency of the triple-quantum excitation.   This is further investigated in

the numerical simulation section later in the text.

2. Near Rotational Resonance Condition

Near RR conditions ($n\omega_r \approx \omega_1$), the states $|p,N,M\rangle$ and $|p',N+Kn,M-K\rangle$ are degenerate (where K is an integer), and H_F must be diagonalized explicitly in these subspaces. For the perturbation treatment to be valid, the energy difference between the states in different nearly degenerate subspaces must be greater than the coupling between those states. H_F can be written as:

$$H_F = H_{deg} + H_{nondeg} \qquad [19]$$

where H_{deg}, which represents the portion of the H_F that must be diagonalized explicitly, is given by:

$$H_{deg} = \omega_r N^r + \omega_1 N^1 + \frac{\sqrt{3}}{2}\omega_1\left[(A_n + iB_n)|T+\rangle\langle C+|(a^+)^n b + (A_{-n} - iB_{-n})|C+\rangle\langle T+|a^n b^+\right] +$$

$$\frac{\sqrt{3}}{2}\omega_1\left[(A_n - iB_n)|C-\rangle\langle T-|(a^+)^n b + (A_{-n} + iB_{-n})|T-\rangle\langle C-|a^n b^+\right] \qquad [20]$$

H_{nondeg}, which represents the interactions between nondegenerate subspaces, is given by:

$$H_{nondeg} = H_{0,1}b^+ + H_{0,-1}b + H_{n,1}(a^+)^n b^+ + H_{-n,-1}a^n b$$

$$+ \sum_{r \neq n > 0} H_{r,1}(a^+)^r b^+ + H_{-r,-1}a^r b + H_{-r,1}a^r b^+ + H_{r,-1}(a^+)^r b \qquad [21]$$

H_{deg} can be diagonalized to give:

$$H_{deg} = \sum_{N=-\infty}^{\infty}\sum_{M=-\infty}^{\infty} (E_{N,M} + \Delta_n + \delta_\Psi^n)|\Psi_{N,M}^+\rangle\langle\Psi_{N,M}^+| + (E_{N,M} + \Delta_n - \delta_\Psi^n)|\Psi_{N,M}^-\rangle\langle\Psi_{N,M}^-|$$

$$+ (E_{N,M} - \Delta_n + \delta_\Phi^n)|\Phi_{N,M}^+\rangle\langle\Phi_{N,M}^+| + (E_{N,M} - \Delta_n - \delta_\Phi^n)|\Phi_{N,M}^-\rangle\langle\Phi_{N,M}^-|$$

where $\Delta_n = \dfrac{n\omega_r - \omega_1}{2}$, $\delta_\Psi^n = \dfrac{1}{2}\sqrt{4\Delta_n^2 + 3\omega_1^2 |A_n + iB_n|^2}$ and

$$\delta_\Phi^n = \frac{1}{2}\sqrt{4\Delta_n^2 + 3\omega_1^2 |A_n - iB_n|^2} \text{ , and}$$

$$\left|\Psi_{N,M}^{+}\right\rangle = \cos(\theta_{\Psi})\left|C+, N, M\right\rangle + \exp(-i\varphi_{\Psi})\sin(\theta_{\Psi})\left|T+, N+n, M-1\right\rangle$$

$$\left|\Psi_{N,M}^{-}\right\rangle = \sin(\theta_{\Psi})\left|C+, N, M\right\rangle - \exp(-i\varphi_{\Psi})\cos(\theta_{\Psi})\left|T+, N+n, M-1\right\rangle$$

$$\left|\Phi_{N,M}^{+}\right\rangle = \cos(\theta_{\Phi})\left|C-, N, M\right\rangle + \exp(-i\varphi_{\Phi})\sin(\theta_{\Phi})\left|T-, N-n, M+1\right\rangle$$

$$\left|\Phi_{N,M}^{-}\right\rangle = \sin(\theta_{\Phi})\left|C-, N, M\right\rangle - \exp(-i\varphi_{\Phi})\cos(\theta_{\Phi})\left|T-, N-n, M+1\right\rangle$$

$$\cos(\theta_{\Psi}) = \frac{\left|A_n + iB_n\right|}{\sqrt{(\delta_{\Psi}^n + \Delta_n)^2 + \left|A_n + iB_n\right|^2}}$$

$$\sin(\theta_{\Psi}) = \frac{\delta_{\Psi}^n + \Delta_n}{\sqrt{(\delta_{\Psi}^n + \Delta_n)^2 + \left|A_n + iB_n\right|^2}}$$

$$\cos(\theta_{\Phi}) = \frac{\left|A_n - iB_n\right|}{\sqrt{(\delta_{\Phi}^n - \Delta_n)^2 + \left|A_n - iB_n\right|^2}}$$

$$\sin(\theta_{\Phi}) = \frac{\delta_{\Phi}^n - \Delta_n}{\sqrt{(\delta_{\Phi}^n - \Delta_n)^2 + \left|A_n - iB_n\right|^2}}$$

$$\exp(i\varphi_{\Psi}) = \frac{A_{-n} - iB_{-n}}{|A_n + iB_n|}$$

$$\exp(i\varphi_{\Phi}) = \frac{A_n - iB_n}{|A_n - iB_n|} \qquad\qquad [22]$$

Starting with initial x-phase CT coherence, $\rho_F(0) = I_X^{2-3}\sum_{NM}\left|N, M\right\rangle\left\langle N, M\right|$, the density

matrix can be rewritten as:

$$\rho_F(0) = I_X^{2-3}\sum_{N,M}\left|N, M\right\rangle\left\langle N, M\right| = \frac{1}{2}\sum_{N,M}\left|C+, N, M\right\rangle\left\langle C+, N, M\right| - \left|C-, N, M\right\rangle\left\langle C-, N, M\right|$$

$$= \frac{1}{2}\sum_{N,M}\cos^2(\theta_{\Psi})\left|\Psi_{N,M}^{+}\right\rangle\left\langle\Psi_{N,M}^{+}\right| + \sin^2(\theta_{\Psi})\left|\Psi_{N,M}^{-}\right\rangle\left\langle\Psi_{N,M}^{-}\right| +$$

$$\cos(\theta_\Psi)\sin(\theta_\Psi)\left(\left|\Psi_{N,M}^-\right\rangle\left\langle\Psi_{N,M}^+\right|+\left|\Psi_{N,M}^+\right\rangle\left\langle\Psi_{N,M}^-\right|\right)-\frac{1}{2}\sum_{N,M}\cos^2(\theta_\Phi)\left|\Phi_{N,M}^+\right\rangle\left\langle\Phi_{N,M}^+\right|$$

$$+\sin^2(\theta_\Phi)\left|\Phi_{N,M}^-\right\rangle\left\langle\Phi_{N,M}^-\right|+\cos(\theta_\Phi)\sin(\theta_\Phi)\left(\left|\Phi_{N,M}^-\right\rangle\left\langle\Phi_{N,M}^+\right|+\left|\Phi_{N,M}^+\right\rangle\left\langle\Phi_{N,M}^-\right|\right) \qquad [23]$$

$\rho_F(t)$, to the lowest order in perturbation theory is:

$$=\frac{1}{2}\sum_{N,M}\cos^2(\theta_\Psi)\left|\Psi_{N,M}^+\right\rangle\left\langle\Psi_{N,M}^+\right|+\sin^2(\theta_\Psi)\left|\Psi_{N,M}^-\right\rangle\left\langle\Psi_{N,M}^-\right|$$

$$+\cos(\theta_\Psi)\sin(\theta_\Psi)\left(\exp(2i\delta_\Psi^n t)\left|\Psi_{N,M}^-\right\rangle\left\langle\Psi_{N,M}^+\right|+\exp(-2i\delta_\Psi^n t)\left|\Psi_{N,M}^+\right\rangle\left\langle\Psi_{N,M}^-\right|\right)$$

$$-\frac{1}{2}\sum_{N,M}\cos^2(\theta_\Phi)\left|\Phi_{N,M}^+\right\rangle\left\langle\Phi_{N,M}^+\right|+\sin^2(\theta_\Phi)\left|\Phi_{N,M}^-\right\rangle\left\langle\Phi_{N,M}^-\right|+$$

$$\cos(\theta_\Phi)\sin(\theta_\Phi)\left(\exp(2i\delta_\Phi^n t)\left|\Phi_{N,M}^-\right\rangle\left\langle\Phi_{N,M}^+\right|+\exp(-2i\delta_\Phi^n t)\left|\Phi_{N,M}^+\right\rangle\left\langle\Phi_{N,M}^-\right|\right) \qquad [24]$$

In Hilbert space, the reduced density matrix for the spin is given by[20]

$$\rho(t)=V(t)\sum_{N,M}\sum_{N',M'}\left\langle N,M\left|\rho_F(t)\right|N',M'\right\rangle\exp(i(N-N')\omega_r t+(M-M')\omega_1 t)V^\dagger(t) \quad [25]$$

From the density matrix, the following expectation values can be calculated:

$$\left\langle I_X^{1-4}\right\rangle(t)=\mathrm{Trace}[I_X^{1-4}\rho(t)]$$

$$=\frac{1}{2}\sin^2(\theta_\Phi)\cos^2(\theta_\Phi)[1-\cos(2\delta_\Phi^n t)]+\frac{1}{2}\sin^2(\theta_\Psi)\cos^2(\theta_\Psi)[1-\cos(2\delta_\Psi^n t)]$$

$$\left\langle I_Y^{1-4}\right\rangle(t)=\mathrm{Trace}[I_Y^{1-4}\rho(t)]=0$$

$$\left\langle I_Z^{1-4}\right\rangle(t)=\mathrm{Trace}[I_Z^{1-4}\rho(t)]=0 \qquad [26]$$

From this expression, it can be seen only that only x-phase triple-quantum coherence (I_X^{1-4}) is created for each orientation. The coefficient in front of $\left\langle I_X^{1-4}\right\rangle$ is always positive. $\left\langle I_X^{1-4}\right\rangle$ is maximal when $\Delta_n=0$ (at RR) and is minimal when $\Delta_n\gg 1$ (away from RR).

CT to triple quantum coherence transfer is also possible from the initial condition

$\rho(0) = I_Y^{2-3}$. Taking $\Delta_n = 0$, a similar calculation shows that, starting with

$\rho_F(0) = I_Y^{2-3} \sum_{N,M} |N,M\rangle\langle N,M|$, the following expectation values can be calculated:

$$\langle I_X^{1-4}\rangle(t) = \text{Trace}[I_X^{1-4}\rho(t)] = 0$$

$$\langle I_Y^{1-4}\rangle(t) = \text{Trace}[I_Y^{1-4}\rho(t)] = \frac{1}{2}\sin(\delta_\Psi^n t)\sin(\delta_\Phi^n t)\cos(\varphi_\Psi - \varphi_\Phi)$$

$$\langle I_Z^{1-4}\rangle(t) = \text{Trace}[I_Z^{1-4}\rho(t)] = -\frac{1}{2}\sin(\delta_\Psi^n t)\sin(\delta_\Phi^n t)\sin(\varphi_\Psi - \varphi_\Phi) \qquad [27]$$

However, the efficiency for $I_Y^{2-3} \to I_Y^{1-4}$ is less than that for $I_X^{2-3} \to I_X^{1-4}$ since the

polarization vector for the states $|1\rangle$ and $|4\rangle$ lies in the Y-Z plane with crystallite-

dependent phase given by $\varphi_\Psi - \varphi_\Phi$ (Eq. [27]). That is, although the CT coherence is

transferred to triple-quantum coherence, cancellation occurs due to powder averaging.

This will be verified numerically in Section III. In addition, starting with the initial

density matrix $\rho_F(0) = 3I_Z^{1-4} \sum_{N,M} |N,M\rangle\langle N,M|$, a similar calculation as above gives the

following expectation values:

$$\langle I_X^{1-4}\rangle(t) = \text{Trace}[I_X^{1-4}\rho(t)] = 0$$

$$\langle I_Y^{1-4}\rangle(t) = \text{Trace}[I_Y^{1-4}\rho(t)] = -\frac{3}{2}\sin(\delta_\Psi^n t + \delta_\Phi^n t)[\sin^2(\theta_\Psi)\cos^2(\theta_\Phi) - \cos^2(\theta_\Psi)\sin^2(\theta_\Phi)]$$

$$-\frac{3}{2}\sin(\delta_\Psi^n t - \delta_\Phi^n t)[\sin^2(\theta_\Psi)\sin^2(\theta_\Phi) - \cos^2(\theta_\Psi)\cos^2(\theta_\Phi)]$$

$$\langle I_Z^{1-4}\rangle(t) = \text{Trace}[I_Z^{1-4}\rho(t)] = \frac{3}{2}\cos(\delta_\Psi^n t + \delta_\Phi^n t)[\cos^2(\theta_\Psi)\sin^2(\theta_\Phi) + \sin^2(\theta_\Psi)\cos^2(\theta_\Phi)]$$

$$+ \frac{3}{2}\cos(\delta_\Psi^n t - \delta_\Phi^n t)[\cos^2(\theta_\Psi)\cos^2(\theta_\Phi) + \sin^2(\theta_\Psi)\sin^2(\theta_\Phi)] \qquad [28]$$

At RR conditions, $\cos(\theta_\Psi) = \cos(\theta_\Phi) = \sin(\theta_\Psi) = \sin(\theta_\Phi) = \frac{1}{\sqrt{2}}$, and hence $\langle I_Y^{1-4}\rangle(t) = 0$

for all times t at this order of perturbation theory. Therefore the triple-quantum excitation efficiency is predicted to be minimal at RR conditions.

C. Spin I > 3/2

For spin I > 3/2, similar predictions are possible. Analogous transformations can be made for higher spins. However, the dynamics are more complicated since there are additional transitions present. Using the above theory, predictions can be made for the spin-locking of the CT. The rotating frame Hamiltonian of a quadrupolar spin I, evolving during MAS and spin-locking irradiation, is given by:

$$H(t) = \omega_Q(t)(3I_Z^2 - I(I+1)) + H_{RF}^{ST} + \left(I + \frac{1}{2}\right)\omega_1 I_X^{CT} \qquad [29]$$

Upon transforming to the quadrupolar and CT frame, the satellite transition coherences that are adjacent to the CT coherence are modulated at a frequency $\omega = \frac{(2I+1)}{4}\omega_1$. Therefore, the CT coherences will be transformed to adjacent satellite transition coherences when $\omega_1 = \frac{4}{2I+1}n\omega_r$. In accordance with our predictions, previous studies have found that under these conditions, the spin-locking efficiency of the CT is minimal (in the absence of second-order quadrupolar effects).[6, 7] Further investigations of transfers between CT coherence and nonadjacent satellite transition coherences are currently under way.

III. NUMERICAL SIMULATION RESULTS

A. Excitation of Triple Quantum Coherences

Fig. 3 shows [(a), (d)] $\left|\left\langle I_-^{1-4}\right\rangle\right|$, [(b), (e)] $\left\langle I_X^{1-4}\right\rangle$, and [(c), (f)] $\left\langle I_Y^{1-4}\right\rangle$, from the initial

condition $\rho(0) = 3I_Z^{1-4}$ under a spin-locking field along the x direction as a function of

spin-locking time and rf field strength. The parameters used in this calculation were $C_Q =$

2.43 MHz, $\eta = 0$ with $\dfrac{\omega_r}{2\pi} = 20$ kHz.   Simulations were performed with [(a), (b), (c)] and

without [(d), (e), (f)] the second-order quadrupolar interaction. As observed in a previous

study,[8] efficient triple-quantum excitation occurs between RR conditions (e.g. 15 kHz <

$\omega_1/2\pi$ < 25 kHz when $\omega_r/2\pi$ = 20 kHz) in the sudden-passage regime, although the

efficiency is minimal at RR and roughly halfway in between RR conditions (i.e.,

$2\omega_1 = n\omega_r$). The inclusion of the second-order quadrupolar interaction does not change

the basic dependence of the magnitude of triple-quantum excitation as a function of rf

power, but the overall efficiency of the excitation is then diminished due to a dephasing

of the coherence. As predicted in Eq. [17], only I_Y^{1-4} triple-quantum coherence is created

in the absence of the second-order quadrupolar interaction, as shown in Fig. 3(e) and (f).

Also, the powder-averaged nutation frequency changes sign in between RR conditions,

which was predicted in the previous section.

In order to investigate triple-quantum excitation in more detail, simulations were

performed for three crystallite orientations whose quadrupolar interactions have different

time dependences. From Eq. [2], $\omega_Q(t)$ oscillates at $2\omega_r$ for $\beta = 90^o$ when $\eta = 0$. For

small values of β (e.g. 10°), $\omega_Q(t)$ oscillates roughly at ω_r, and for medium values of

β (e.g. 45°), $\omega_Q(t)$ oscillates at both ω_r and $2\omega_r$. Thus, these orientations were chosen to

explore what effects different time dependences of $\omega_Q(t)$ have on the observed triple-quantum excitation.

Fig. 4 shows $\left\langle -I_Y^{1-4} \right\rangle$ for these three crystallite orientations. The second-order quadrupolar interaction is not considered in the following simulations since it does not affect the basic features of the triple-quantum excitation. From Eq. [7], it can be shown by expanding in Bessel functions that for $\beta = 90^o$, $H_{n,\pm 1} \neq 0$ only when n is even, whereas for $\beta = 10^o$ and 45°, $H_{n,\pm 1}$ can be nonzero for all n. At RR conditions (e.g., $\omega_1/2\pi = 20$ for $\beta = 10^o$ and 45° [Fig. 4(b)] and $\omega_1/2\pi = 40$ kHz for $\beta = 10^o$, 45°, and 90° [Fig. 4(f)] respectively), the triple-quantum excitation efficiency is minimal. Away from RR conditions, triple-quantum coherence is created efficiently but with a different optimum condition for each crystallite orientation (Fig. 4(a), 4(c), 4(d), 4(e)). This results in considerable destructive interference in the triple-quantum excitation signal, degrading the overall excitation efficiency for a powdered sample. As seen in Fig. 3, when $\omega_1 \approx (n+1/2)\omega_r$, the efficiency of triple-quantum excitation is near zero, which is consistent with the predictions made in section II. For $\beta = 10^o$, where $\omega_Q(t)$ oscillates at ω_r, a change in the sign of ω_{nut} is seen between $\omega_1/2\pi = 15$ and 25 kHz (Figs. 4(a) and 4(c) respectively). Similar behavior also was observed for $\beta = 90^o$ between $\omega_1/2\pi$ of 35 kHz and 45 kHz. Note also that halfway in between RR conditions, i.e., $\omega_1 = (n+1/2)\omega_r$, excitation efficiency is nonzero for these crystallite orientations [Fig. 4 (d)]; in fact for $\beta = 90^o$, triple-quantum excitation is most efficient at $\omega_1/2\pi = 30$ kHz. However, the powder average of the excitation efficiency vanishes near this condition. This minimum is qualitatively different than those minima occurring at RR conditions, which result from

a mixing of CT coherence states with triple-quantum coherence states (Eq. [28]). These effects will be discussed in the next section.

Although Eq. [17] predicts a simple nutation away from RR conditions, Fig. 4 indicates that the dynamics are more complicated. Inclusion of higher-order terms in the perturbation treatment of Eq. [16] would be necessary in order to quantitatively capture the evolution. Such work is in currently in progress.

B. Conversion of CT Coherence into Triple Quantum Coherence

Fig. 5 shows [(a), (d)] $\left|\left\langle I_-^{1-4}\right\rangle\right|$, [(b), (e)] $\left\langle I_X^{1-4}\right\rangle$, and [(c), (f)] $\left\langle I_Y^{1-4}\right\rangle$ (with [(a), (b), (c)] and without [(d), (e), (f)] considering second-order quadrupole interactions) created from CT coherence (I_X^{2-3}) under the influence of the rf irradiation along the x-direction, as a function of rf power and spin lock time. In contrast to the $I_Z^{1-4} \rightarrow I_-^{1-4}$ transfer, optimum transfer occurs at RR conditions. In the absence of the second-order quadrupolar interaction, only the x-component of triple-quantum coherence, I_X^{1-4}, is created, which is predicted from Eq. [26]. In Fig. 6, $\left\langle I_X^{1-4}\right\rangle$ is shown for the first two RR conditions for three crystallite orientations in the absence of second-order quadrupolar interactions. As predicted in the theory section, effective coherence transfer is induced at RR conditions (i.e. $\omega_1/2\pi = 20$ kHz for $\beta = 10^o$ and 45° and $\omega_1 = 40$ kHz for $\beta = 10^o$, 45°, and 90°). As mentioned in the previous section, RR effects only occur for $\beta=90^o$ when $\omega_1 = 2n\omega_r$, i.e., only even RR conditions occur for this crystallite, whereas both even and odd occur $\beta = 10^o$ and 45°. Note that in Fig. 6, $\left\langle I_X^{1-4}\right\rangle \geq 0$ for all crystallites and for all times, which was predicted from Eq. [26]. In Fig. 7, $\left\langle I_X^{1-4}\right\rangle$ was calculated using

19

Eq. [26] for the three orientations. Fig. 7(a) is in very good with the exact numerical calculation of Fig. 6(a). In Fig. 7(b) the agreement with Fig. 6(b) is not as good; in particular, the predictions for $\beta = 10^{\circ}$ have little resemblance with the exact numerical simulation. Since the theory is just to zeroth-order, higher-order terms are expected to become important in order to quantitatively predict $\left\langle I_X^{1-4} \right\rangle (t)$.

Another aspect of the Hamiltonian under RR conditions is that it can induce coherence transfer between $I_Y^{2-3} \leftrightarrow I_Y^{1-4}$, even though the rf irradiation is along the x-direction. Numerical calculations of the $I_Y^{2-3} \leftrightarrow I_Y^{1-4}$ transfer were performed in order to confirm these predictions. In Fig. 8, $\left| \left\langle I_-^{1-4} \right\rangle \right|$ was calculated over a powder for two different spinning speeds, $\omega_r/2\pi = 20$ kHz [Fig. 8(a)] and $\omega_r/2\pi = 40$ kHz [Fig. 8(b)]. Efficient transfer was not observed for almost all rf powers.

Calculations $I_Y^{2-3} \leftrightarrow I_Y^{1-4}$ were performed for single crystallite orientations in order to check if the inefficiency of the transfer was due to a destructive interference between different crystallite orientations. Fig. 9 shows the simulation results for $I_Y^{2-3} \rightarrow I_Y^{1-4}$ transfers at RR conditions, in the absence of second-order quadrupolar interaction and resonance offsets. Interestingly, efficient transfer does occur for all three crystallite orientations. However, significant destructive interference across the powder is observed for these crystallite orientations even without considering the second-order quadrupole interaction. As seen from Eq. [27] and Fig. 9, the expectation values of triple-quantum coherence can be either positive or negative resulting in a cancellation of the triple-quantum coherence signal in a powdered sample.

IV. CONCLUSIONS

The purpose of this study was to present a theory of the excitation and conversion between multiple-quantum coherences in spin I = 3/2 quadrupolar nuclei in powdered samples in the sudden-passage limit. The theory is applicable to rf irradiation even at RR conditions ($\omega_1 = n\omega_r$) and may be extended to included resonance offset and second-order quadrupolar effects, as well as potentially generalized to the treatment of I > 3/2 nuclei. It may be used to predict the results of the recent FASTER MQMAS experiments[8], as well as the heretofore-unexplained reductions in spin-locking efficiency of the central transition at rotational resonance conditions[6, 7]. A complete analytic theory of this sort has not been presented elsewhere. In this work, the spin-locking Hamiltonian was first transformed into a novel combined quadrupolar and CT interaction frame and then rendered time-independent via a bimodal Floquet treatment. At this point, perturbation theory was used in order to describe the spin dynamics at and away from RR. At RR conditions, the conversion of CT coherence to triple-quantum coherence was found to be efficient over a powdered sample. When the phase of the rf irradiation is along the x-direction, $I_X^{2-3} \rightarrow I_X^{1-4}$ is efficient over the powder; however, $I_Y^{2-3} \rightarrow I_Y^{1-4}$ is inefficient due to the fact that the signals from different crystallites destructively interfere, resulting in an overall degradation of the coherence transfer efficiency. Away from RR conditions, the excitation of triple-quantum coherence from z-magnetization was found to be efficient, and minimal excitation occurs for most crystallites when at RR. However, when roughly halfway in between RR conditions, the overall excitation efficiency also was found to be minimal, this time due to a cancellation of signals over the powder.

In future work, the theory will be extended to higher-orders of perturbation theory since the energy difference between the Floquet states is not much greater than the coupling between them, necessitating the inclusion of higher-order corrections into the theory. Also, the calculation of higher-order perturbation terms will be necessary in order to understand the dynamics of I>3/2 nuclei in the sudden-passage limit, such as five-quantum coherence creation and the corresponding multiple-quantum conversions. Further theoretical and experimental studies are currently underway.

REFERENCES

1   L. Frydman, and J.S. Harwood, *J. Am. Chem. Soc*. **117**, 5367 (1995).

2   A. Medek, J.S. Harwood, and L. Frydman, *J. Am. Chem. Soc*. **117**, 12779 (1995).

3   A.J. Vega, *J. Magn. Reson*. **96**, 50 (1992)

4   A.J. Vega, *Solid State Nucl. Magn. Reson.* **1**, 17 (1992)

5   G. Wu, D. Rovnyak, and R.G. Griffin, *J. Am. Chem. Soc.* **118**, 9326 (1996)

6   W. Sun, J.T. Stephen, L.D. Potter, and Y. Wu, *J. Magn. Reson. Ser. A* **116**, 181 (1995)

7   S.M. DePaul, M. Ernst, J.S. Shore, J.F. Stebbins, and A. Pines, *J. Phys. Chem. B* **101**, 3240 (1997)

8   T. Vosegaard, P. Florian, D. Massiot, and P.J. Grandinetti, *J. Chem. Phys* **114**, 4618 (2001)

9   E. Vinogradov, P.K. Madhu, and S. Vega, *Chem. Phys. Lett*. **329**, 207 (2000)

10   S. Vega and A. Pines, *J. Chem. Phys*. **66**, 5624 (1977)

11   S. Vega, *J. Chem. Phys*. **68**, 5518 (1978)

12 G. Jeschke, *J. Chem. Phys*. **108**, 907 (1998)

13   Y. Zhang, F. Deng, J.Q. Qiu, and C.H. Ye, *Solid State Nucl. Magn. Reson.* **15**, 209 (2000)

14   P.K. Madhu, A. Goldbourt, L. Frydman, and S. Vega, *J. Chem. Phys*, **112**, 237 (2000)

15   M. Eden and L. Frydman, *J. Chem. Phys*. **114**, 4116 (2001)

16   S. Ding and C.A. McDowell, *Mol. Phys*. **95**, 841 (1998)

17   J.H. Shirley, *Phys. Rev*. **138**, 979 (1965)

18 A. Llor, *Chem. Phys. Lett.*, **199**, 383 (1992)

19 M. Bak and N.C. Nielsen, *J. Magn. Reson*. **125**, 132 (1997)

20 T. O. Levante, M. Baldus, B.H. Meier, and R.R. Ernst, *Mol. Phys.* **86**, 1195

(1995)

FIGURE CAPTIONS:

Figure 1. The fraction of crystallite orientations satisfying Eq. [15] as a function of rf field strength, ω_1. For $\eta = 0$ and C_Q= 2.43 MHz, 2000 pairs of powder angles (β, γ) were generated using the REPULSION sampling.[19] The Fourier coefficients A_N and B_N of Eq. [7] were generated for these angles up to $|N| = 80$. Eq. [7] was then directly evaluated for each orientation. Spinning speeds of $\omega_r/2\pi = 20$ kHz [(a), (c)] and $\omega_r/2\pi = 40$ kHz [(b), (d)] were examined. The number of crystallites satisfying the condition $\left|(N - N')\omega_r \pm \omega_1\right| > 2\left|H_{N-N',\pm 1}\right|$ for all N and N' are presented in (a) and (b) while those satisfying the condition $\left|(N - N')\omega_r \pm \omega_1\right| > 4\left|H_{N-N',\pm 1}\right|$ for all N and N' are shown in (c) and (d). RR conditions are shown with a dotted line. As ω_1 increases, the number of crystallites satisfying Eq. [15] decreases.

Figure 2. The distribution for -ω_{nut} over a powder calculated from Eq. [18] for various ω_1 values. For $\eta = 0$, C_Q= 2.43 MHz, and $\omega_r/2\pi = 20$ kHz, only those crystallites satisfying the condition $\left|(N - N')\omega_r \pm \omega_1\right| > 2\left|H_{N-N',\pm 1}\right|$ were considered from a set of 2000 powder points. $\omega_1/2\pi$ values of (a) 25 kHz, (b) 30 kHz, (c) 35 kHz, (d) 45 kHz, (e) 50 kHz, and (f) 55 kHz were used. $\dfrac{\overline{\omega_{nut}}}{2\pi}$ is average nutation frequency over the powder, and σ is the standard deviation. From the distributions it can be seen that the mean value of the distribution shifts from positive to negative in between RR conditions, passing through zero roughly midway.

Figure 3. Exact numerical calculation of [(a), (d)] $\left|\left\langle I_-^{14}\right\rangle\right|$, [(b), (e)] $\left\langle I_X^{1-4}\right\rangle$, and [(c), (f)] $\left\langle -I_Y^{1-4}\right\rangle$ under rf irradiation along the x-direction applied to $\rho(0) = 3I_Z^{1-4}$, with [(a), (b), (c)] and without [(d), (e), (f)] considering the second-order quadrupolar interaction, as a function of rf power and pulse length. The parameters used in the simulation were $\eta = 0$, and C_Q= 2.43 MHz. A total of 1154 crystallite orientations were employed at a $\omega_r/2\pi =$ 20 kHz for the powder average. RR conditions are shown with a dotted line. Equally spaced contour levels are shown (with dashed contours indicating negative values) in the following ranges: (a) {0.1, 0.45}, (b) {-0.3, 0.3}, (c) {-0.15, 0.2}, (d) {0.15, 0.6}, (e) $\{-6\times10^{-14}, 3\times10^{-14}\}$, and (f) {-0.3, 0.5}.

Figure 4. Exact numerical calculation of $\left\langle -I_Y^{1-4}\right\rangle$ for the three crystallite orientations ($\beta =$ 10° (dashed line), $\beta = 45°$ (dotted line), and $\beta = 90°$ (solid line)) created from $\rho(0) =$ $3I_Z^{1-4}$ at various rf powers: (a) 15, (b) 20, (c) 25, (d) 30, (e) 35, and (f) 40 kHz. The parameters used in the simulation were $\omega_r/2\pi = 20$ kHz, $\eta = 0$, and C_Q= 2.43 MHz. In particular, note that (d), excitation is efficient for both $\beta = 90°$ and $\beta = 10°$, as contrasted to excitation at RR conditions in (b) (for $\beta = 10°$ and 45°) and (f) ($\beta = 10°$, 45°, and 90°) where the excitation efficiency is minimal.

Figure 5. Exact numerical calculation of [(a), (d)] $\left|\left\langle I_-^{14}\right\rangle\right|$, [(b), (e)] $\left\langle I_X^{1-4}\right\rangle$, and [(c), (f)] $\left\langle I_Y^{1-4}\right\rangle$, under spin-locking along the x-direction applied to I_X^{2-3}, with [(a), (b), (c)] and without [(d), (e), (f)] considering second-order quadrupolar interaction, as a function of

the rf power and pulse length. The parameters in the simulation were $\omega_r/2\pi = 20$ kHz, $\eta = 0$, and C_Q= 2.43 MHz. A total of 1154 crystallite orientations were employed in the calculation. Equally spaced contour levels are shown (with dashed contours indicating negative) in the following ranges: (a) {0.06, 0.24}, (b) {0.02, 0.22}, (c) {-.12, 0}, (d) {0.06, 0.24}, (e) {0.06, 0.24}, and (f) $\{-1.2\times10^{-14}, 2\times10^{-15}\}$. Only the first two RR conditions, $\omega_1 = \omega_r$ and $\omega_1 = 2\omega_r$ were observed for these parameters [(a), (d)], and, as shown in (e), only efficient transfer was observed for $I_X^{2-3} \rightarrow I_X^{1-4}$ [(b), (e)], with $\langle I_X^{1-4} \rangle \geq 0$ for all time and ω_1.in the absence of second-order quadrupolar interaction. As shown in (f), $I_X^{2-3} \rightarrow I_Y^{1-4}$ is negligible over the powder in the absence of second-order quadrupolar interaction. RR conditions are marked with a dotted line.

Figure 6. Exact numerical calculation of $\langle I_X^{1-4} \rangle$ for three orientations ($\beta = 10^o$ (dashed line), $\beta = 45^o$ (dotted line), and $\beta = 90^o$ (solid line)) from I_X^{2-3} at rf field strengths of (a) $\omega_1/2\pi$= 20 and (b) $\omega_1/2\pi$= 40 kHz in the absence of second-order quadrupolar coupling. The parameters used in the simulation were $\omega_r/2\pi = 20$ kHz, $\eta = 0$, and C_Q= 2.43 MHz. Again, $\langle I_X^{1-4} \rangle \geq 0$ for all three orientations, as predicted in Eq. [26].

Figure 7. Calculation of $\langle I_X^{1-4} \rangle$ for three orientations ($\beta = 10^o$ (dashed line), $\beta = 45^o$ (dotted line), and $\beta = 90^o$ (solid line)) from I_X^{2-3} at rf field strengths of (a) $\omega_1/2\pi$= 20 and (b) $\omega_1/2\pi$= 40 kHz using Eq. [26]. The parameters used were $\omega_r/2\pi = 20$ kHz, $\eta = 0$, and
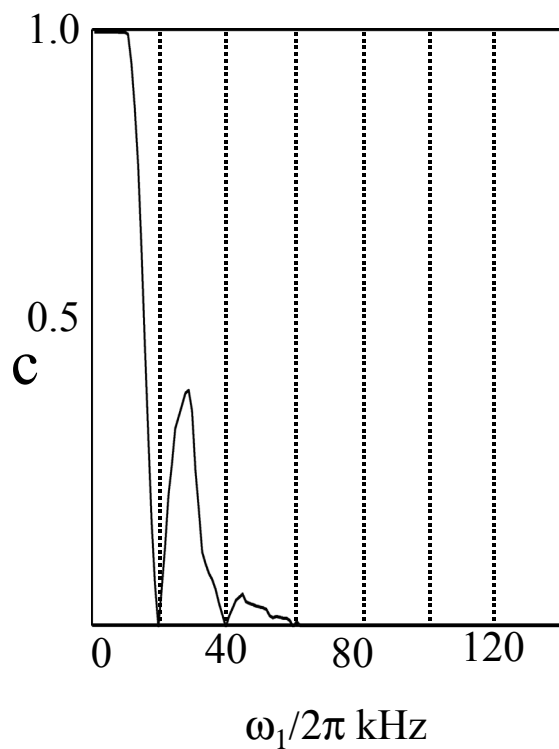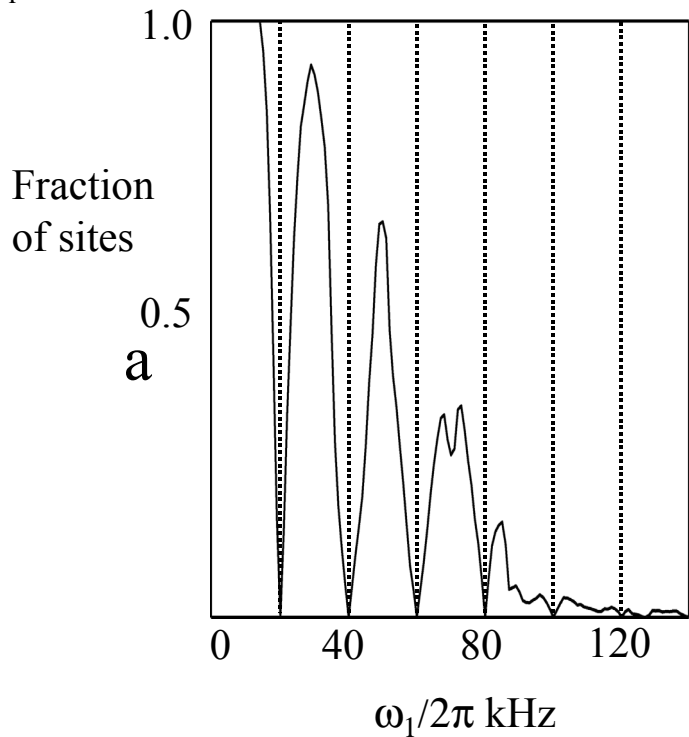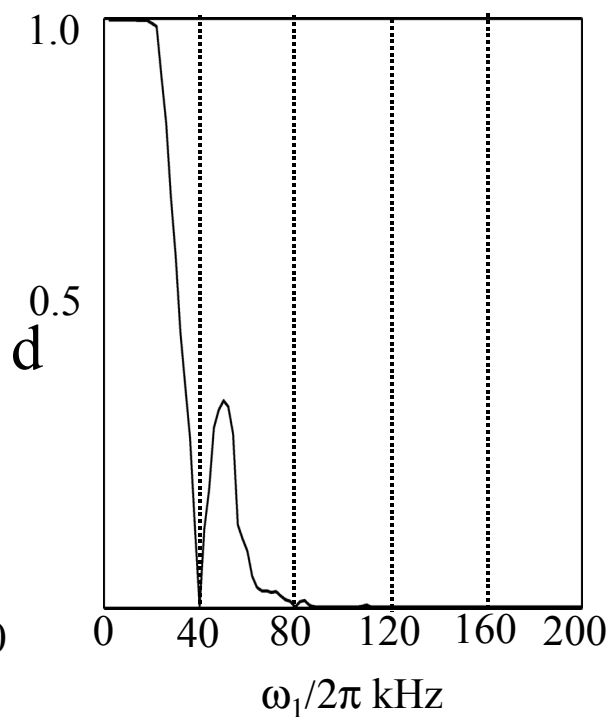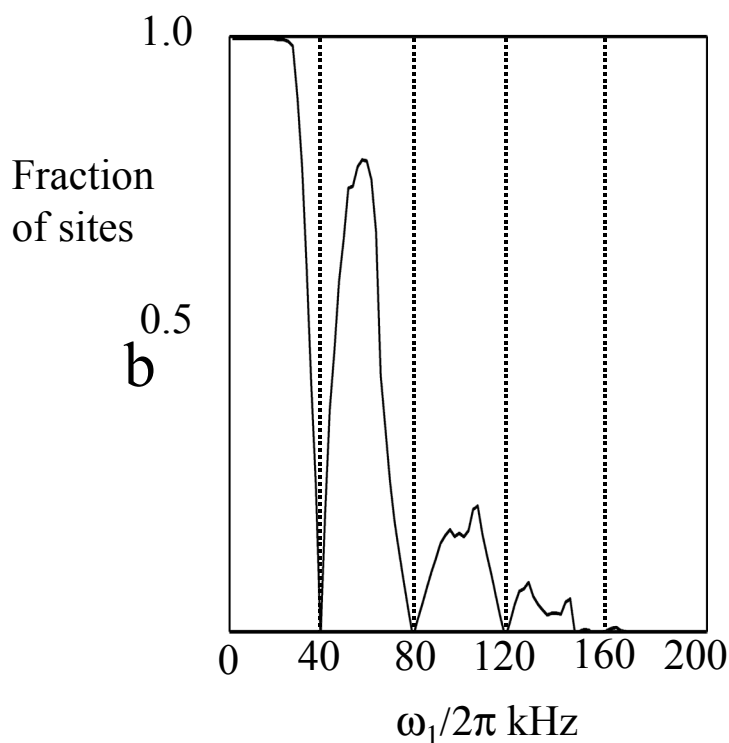
C_Q= 2.43 MHz. Eq. [26] is able to predict many of the features in the exact numerical simulation of Fig. 6.

Figure 8. Exact numerical calculation of $\left| I_-^{1-4} \right|$ under rf irradiation along the x-direction applied to I_Y^{2-3} (a) with and (b) without considering second-order quadrupole interaction, as a function of the rf power and pulse length. The parameters used in the simulation were $\omega_r/2\pi = 20$ kHz, $\eta = 0$, and C_Q= 2.43 MHz. Equally spaced contour lines are shown with between {0.012, 0.026}. A total of 1154 crystallite orientations were employed in the simulation, and RR conditions are marked with a dotted line.

Figure 9. Exact numerical calculation of $\left\langle -I_Y^{1-4} \right\rangle$ for the three orientations (β = 10° (dashed line), β = 45° (dotted line), and β = 90° (solid line)) from $\rho(0) = I_Y^{2-3}$ at rf field strengths of (a) $\omega_1/2\pi$ = 20 and (b) $\omega_1/2\pi$ = 40 kHz. The parameters used in the simulation were $\omega_r/2\pi = 20$ kHz, $\eta = 0$, and C_Q= 2.4 MHz.

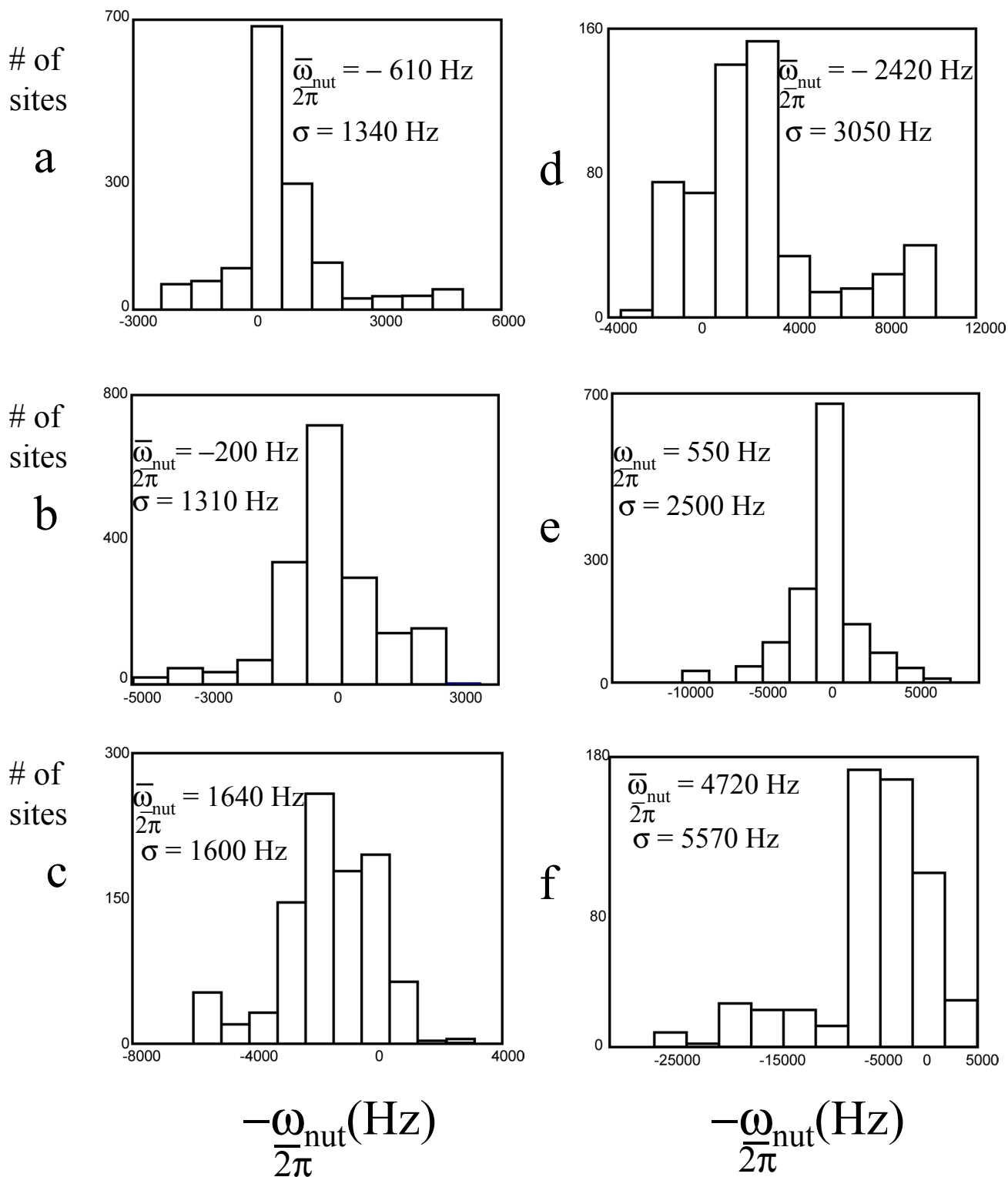# J. Walls, K.H. Lim, & A. Pines Figure 1

J. Walls, K.H. Lim, & A. Pines Figure 2
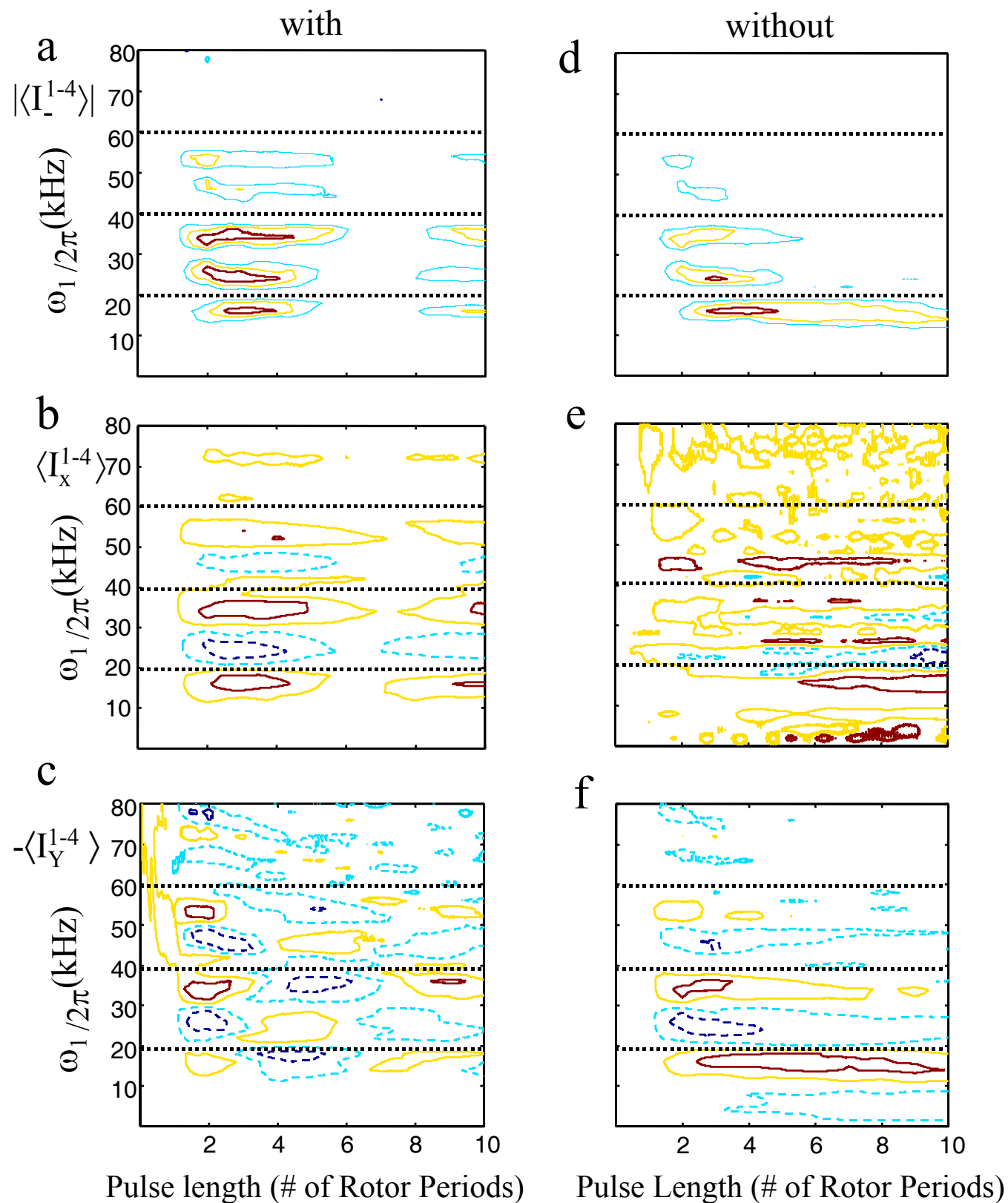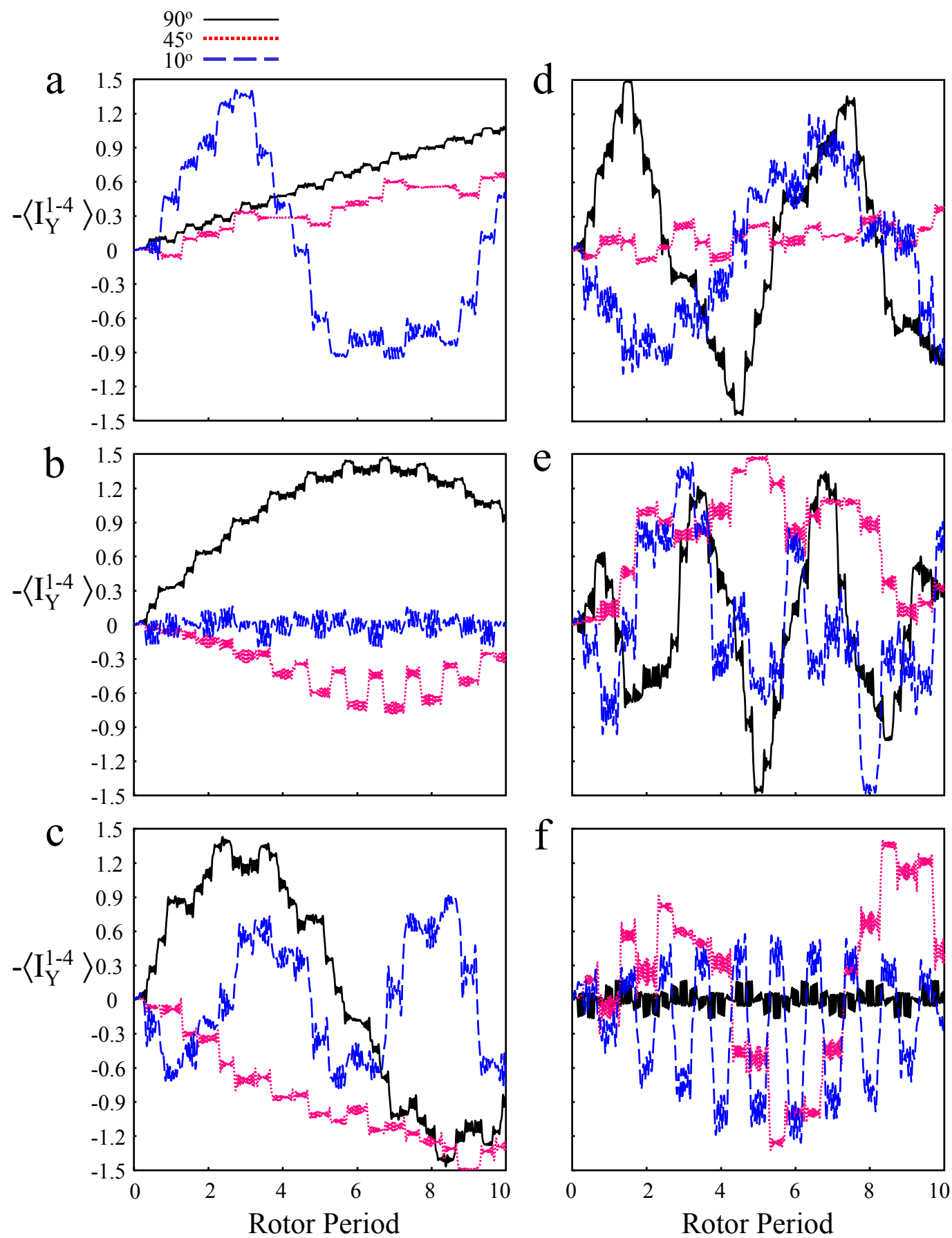
J. Walls, K.H. Lim, & A. Pines Figure 3

J. Walls, K.H. Lim, & A. Pines Figure 4

with

without

a

$|\langle I_-^{1-4} \rangle|$

$\omega_{1/2\pi}(\text{kHz})$

d

b

$\langle I_x^{1-4} \rangle$

$\omega_{1/2\pi}(\text{kHz})$
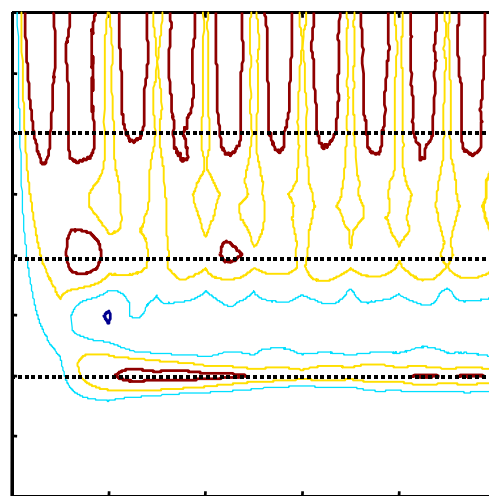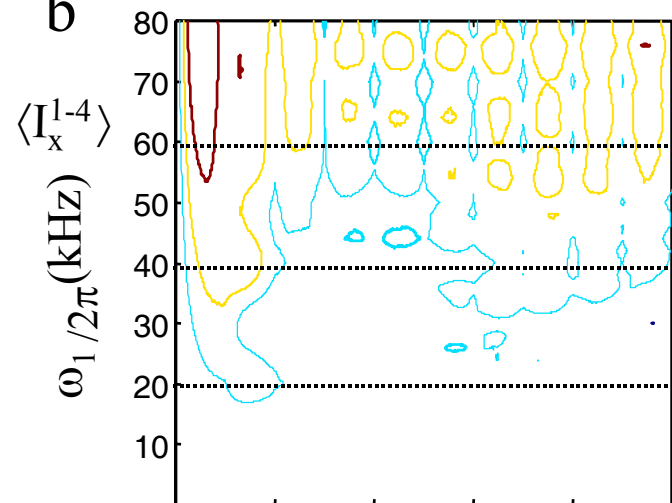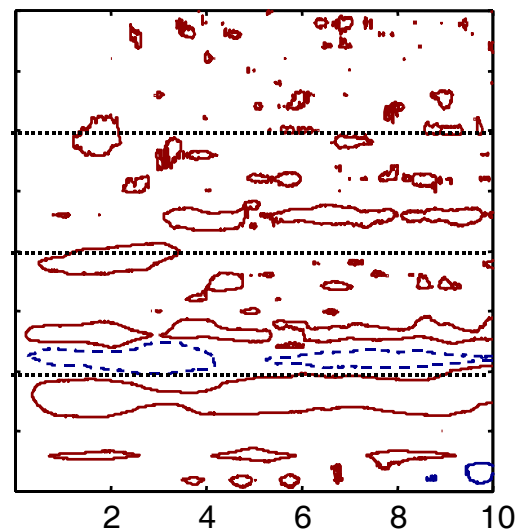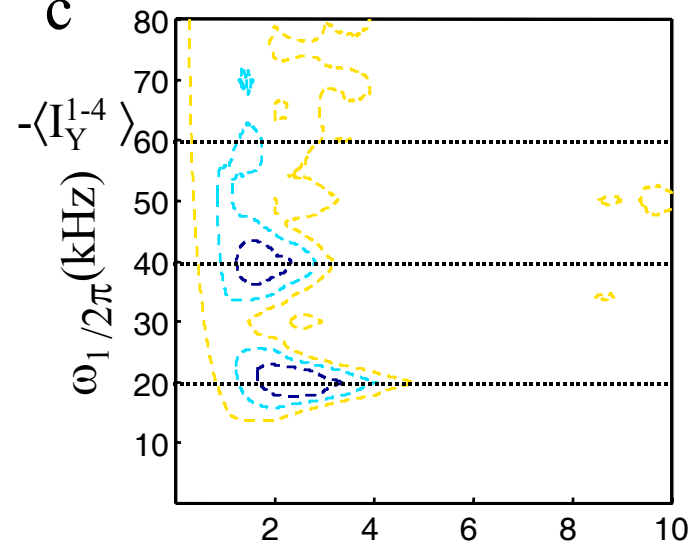
e

c

$-\langle I_Y^{1-4} \rangle$

$\omega_{1/2\pi}(\text{kHz})$
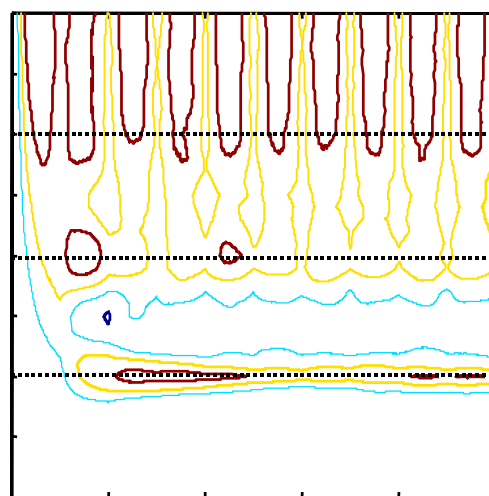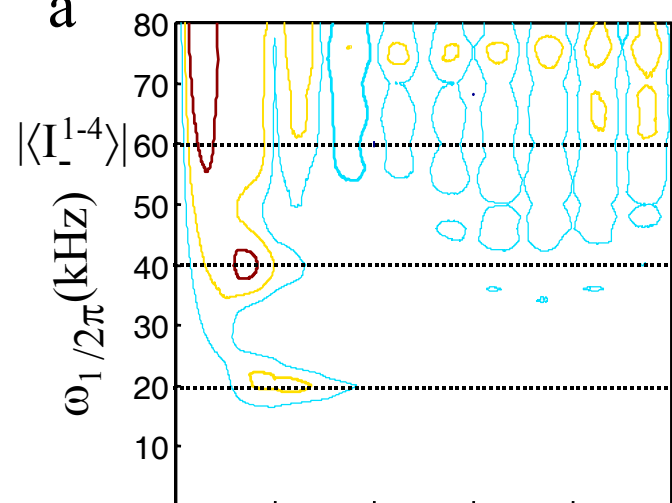
f

Pulse Length (# of Rotor Periods)

Pulse Length (# of Rotor Periods)

J. Walls, K.H. Lim, & A. Pines Figure 6

J. Walls, K.H. Lim, & A. Pines Figure 7

J. Walls, K.H. Lim, & A. Pines Figure 9